Enhanced magnetoelectric effect by spin-orbit coupling in M-type hexaferrite

Ye Shao, Lihuai Shu, Fengzhen Huang,* Shuo Yan, Xiaomei Lu,† and Jinsong Zhu
National Laboratory of Solid State Microstructures and Physics School, Nanjing University, Nanjing 210093, China

(Received 1 May 2022; revised 31 August 2022; accepted 4 October 2022; published 18 October 2022)

Magnetoelectric (ME) effect triggered by spiral spin orders in various hexaferrites develops both the theory and application of ME coupling. However, the strength of such ME effect is restricted by the small spin-orbit coupling (SOC) of 3*d* electrons in M-type hexaferrite. Here, we introduce the 5*d* element Ir with large SOC into $SrFe_{12}O_{19}$. It is found that a low Ir^{4+}-doping level (about 4.2% of total Fe^{3+} ions) can induce conical spin order in $SrMg_xIr_xFe_{12-2x}O_{19}$ ceramics, mainly because Ir^{4+} ions prefer to enter a crucial $4f_2$ magnetic-interacted site and thus strengthen the local Dzyaloshinskii-Moriya interaction. Spin-order-induced polarization (P_{spin}) is achieved and displays a synchronous temperature-dependent behavior with the displacive polarization (P_{disp}). This interesting ME effect is discussed via *d*-*p* hybridization emerging at FeO_5 trigonal bipyramids. Moreover, P_{spin} response decreases step by step during the periodical ME test, reflecting the controllable helicity and the possible multilevel states. These results demonstrate the impact of the 5*d* element with strong SOC on the formation of conical spin order and the enhancement of ME effect in M-type hexaferrite, and also reveal the interconnectedness between P_{spin} and P_{disp}.

DOI: 10.1103/PhysRevB.106.144419

I. INTRODUCTION

Magnetoelectric (ME) coupling triggered by spiral spin orders has drawn physical and technological interests in hexaferrite families, involving M-type [1–3], Y-type [4–6], and Z-type [6–8] hexaferrites. Among them, M-type hexaferrite (Ba, Sr)$Fe_{12}O_{19}$ has been commercially employed due to its excellent magnetic properties and low cost [9]. As shown in Fig. 1(a), (Ba, Sr)$Fe_{12}O_{19}$ belongs to magnetoplumbite structure, and Fe^{3+} ions are distributed in three kinds of octahedral sites (2*a*, $4f_2$, and 12*k*), one tetrahedral site ($4f_1$), and one trigonal bipyramidal site (2*b*) [9]. Generally, in centrosymmetric magnetoplumbite structure, Fe^{3+} ions of the trigonal bipyramid site should lie in the equatorial plane, while they are displaced out of the plane according to Mössbauer spectroscopy and x-ray diffraction study [10,11]. Such displacement not only exists at room temperature but also usually larger than that at lower temperature [12]. Shen *et al.* suggested that the competition between the long-range Coulomb interaction and short-range Pauli repulsion in the FeO_5 bipyramidal favors the off-center displacement of Fe^{3+} at the 2*b* site [13], contributing to the corresponding quantum paraelectric behavior of (Ba, Sr)$Fe_{12}O_{19}$ and the displacive polarization (P_{disp}) [13–16]. While the spin-order-induced polarization (P_{spin}), which is commonly induced by spiral spin orders via inverse Dzyaloshinskii-Moriya interaction (DMI) or the metal-ligand *d*-*p* hybridization model [17–19], is more fascinating in (Ba, Sr)$Fe_{12}O_{19}$-based materials [1–3]. However, the strict threefold rotation symmetry of the (Ba, Sr)$Fe_{12}O_{19}$ lattice limits the emergence of spiral spin order since the related antisymmetric DMI [$\boldsymbol{D}_{ij} \cdot (\boldsymbol{S}_i \times \boldsymbol{S}_j)$] is totally compensated [3]. Recently, conical spin order and the related ferroelectricity are reported when about 16% of Fe^{3+} ions are substituted by nonmagnetic Sc^{3+} or In^{3+} ions [1,3,20,21], since Sc^{3+}/In^{3+} doping breaks the threefold symmetry of the (Ba, Sr)$Fe_{12}O_{19}$ lattice and makes a local uncompensated DMI [1,3]. Nonetheless, on the one hand, the ME strength is restricted by the small spin-orbit coupling (SOC) of 3*d* electrons. On the other hand, though both P_{disp} and P_{spin} are vital factors for the practical applications of multiferroic materials, the relationship between them remains a puzzle.

We attempt to focus on the above issue from the point of SOC since it can determine the local DMI [22,23] and contribute to P_{spin} in either an inverse DMI or the *d*-*p* hybridization model [17–19]. The Hamiltonian of SOC is expressed as $H = \zeta \boldsymbol{L} \cdot \boldsymbol{S}$, where ζ denotes the SOC coefficient, $\boldsymbol{L}$ is the orbital angular momentum, and $\boldsymbol{S}$ is the spin. In hexaferrites, Fe^{3+} ions with large spin moments make up spin order, but its SOC is weak due to the small ζ ($\sim$0.1 eV) of 3*d* electrons [24]. Moreover, the orbital moments ($\sim 0.01\,\mu_B$/Fe) are almost quenched for Fe^{3+} ions according to the first-principle calculations of $SrFe_{12}O_{19}$ [25]. The Co^{2+} ion can reserve a sizable orbital moment for its $3d^7$ electronic configuration [26,27], and therefore, (Ba, Sr)$Fe_{12}O_{19}$ doped with Co^{2+}-Ti^{4+} ions usually possesses conical spin order and obvious ME effect [2,15,28]. Compared with Fe^{3+} ions, 5*d* transition-metal Ir^{4+} ions possess large ζ ($\sim$ 0.4 eV) and unquenched orbital moment, and thus

*Author to whom correspondence should be addressed: fzhuang@nju.edu.cn
†Author to whom correspondence should be addressed: xiaomeil@nju.edu.cn

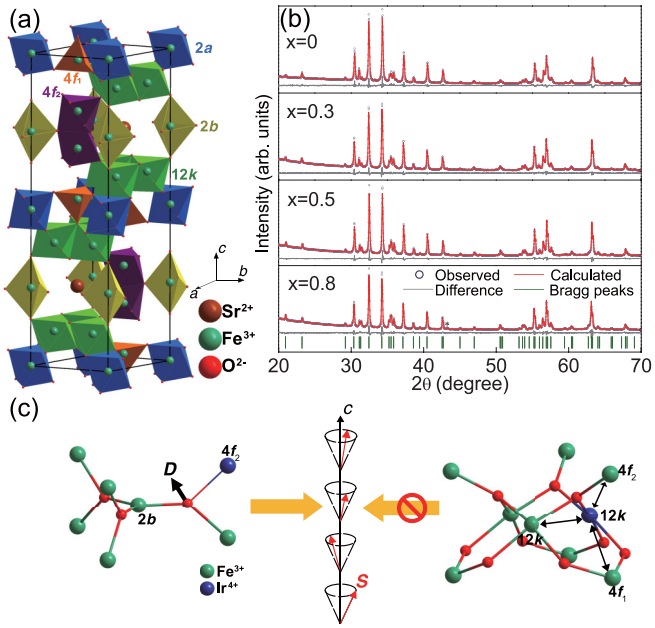

FIG. 1. (a) Schematic of the $SrFe_{12}O_{19}$ crystal structure, (b) XRD patterns of $SrMg_xIr_xFe_{12-2x}O_{19}$ ceramics, and (c) schematic of the relationship between conical spin order and local DMI according to the ionic occupation of $SrMg_xIr_xFe_{12-2x}O_{19}$.

Ir-based compounds have led the edge of spintronics for their fascinating electronic state induced by large SOC [29–32]. Therefore, it is reasonable to believe that the local DMI and thus P_{spin} of (Ba, Sr)$Fe_{12}O_{19}$ can be greatly enhanced if an Ir^{4+} ion is introduced. In this paper, $SrMg_xIr_xFe_{12-2x}O_{19}$ hexaferrite is designed to verify the above expectation, where a Mg^{2+} ion is introduced for charge balance. A conical magnetic structure and enhanced ME effect are obtained in $SrMg_xIr_xFe_{12-2x}O_{19}$ ($x = 0.5$ and 0.8) because of the preferred substitution of Ir^{4+} ions at the crucial $4f_2$ sublattice and its strong SOC. Based on the d-p hybridization model, the magnitude of P_{spin} is revealed to correlate with that of P_{disp}.

II. SAMPLES AND EXPERIMENTAL DETAILS

$SrMg_xIr_xFe_{12-2x}O_{19}$ ($x = 0$, 0.3, 0.5, and 0.8) ceramics were prepared by solid-state reactions. The stoichiometric ratios of $SrCO_3$, MgO, IrO_2, and Fe_2O_3 were mixed via high-energy milling for 24 h and then preheated at 1150 °C for 2 h in O_2 atmosphere. After being milled for 24 h again, the well-mixed powders were pressed into pellets 1.5 mm thick and calcined at 1200 °C–1250 °C for 2 h in O_2 atmosphere. X-ray diffraction with Cu $K\alpha$ radiation (XRD, Bruker D8) was used to characterize the crystal structure. Rietveld refinements for XRD patterns were conducted using the Total Pattern Analysis Solutions (TOPAS, Bruker) program. Scanning electron microscopy (SEM, Quanta 200) was used for analyzing the topographies of the ceramics. X-ray photoelectron spectra (XPS) were collected by a PHI5000 VersaProbe. X-ray absorption spectra (XAS) were carried out at the National Synchrotron Radiation Laboratory, China. The magnetic properties were measured using a commercial magnetic property measurement system (SQUID-VSM, Quantum Design). The magnetic domain patterns were measured by a magnetic force microscope (MFM, Bruker Icon). Prior to the electrical measurement, ceramics were polished to about 0.12 mm thickness and silver paste was painted on both their sides to form a capacitance. ME current was collected by a Keithley 6514 SourceMeter on a physical property measurement system (PPMS, Quantum Design). The ferroelectric hysteresis loops were measured by a Keithley 6517B SourceMeter under a positive-up–negative-down (PUND) method on a PPMS.

III. RESULTS AND DISCUSSION

A. Crystal structures

$SrMg_xIr_xFe_{12-2x}O_{19}$ ceramics are well grown with an average grain size of about 1 μm, as shown in Supplemental Material Fig. S1 [33]. Figure 1(b) presents the XRD patterns of $SrMg_xIr_xFe_{12-2x}O_{19}$ powders ground from the corresponding ceramics. All the ceramics possess magnetoplumbite structure with the $P6_3/mmc$ space group, and the slight secondary spinel phase is marked with *. To figure out the structural details of $SrMg_xIr_xFe_{12-2x}O_{19}$, Rietveld refinement is conducted and the ionic occupation ratios together with the small residual factor-weighted pattern (R_{wp}) and residual factor pattern (R_p) are given in Table I. There are four features worth mentioning, and first, as we know, the ionic scattering ability for x ray determines the intensity of the corresponding diffraction peak. In $SrMg_xIr_xFe_{12-x}O_{19}$ ceramics, the scattering abilities of Mg, Ir, and Fe ions are of great difference due to their different electronic configuration, being responsible for the reliability of Rietveld analysis. Therefore, though the fitting values of different sample batches may be slightly different, their trend with x increase is the same when R_{wp} and R_p are less than 10. Second, for XRD measurement, the displacement of Fe^{3+} either above or below the equatorial plane contributes equally to the diffraction intensity since the equatorial plane of bipyramids is also the mirror of the magnetoplumbite lattice [12]. Therefore, the off-center displacement of the $2b$ site (z_{2b}) can be estimated by Rietveld analysis. As shown in Table I, z_{2b} is about 0.048, 0.065, 0.120, and 0.056 Å for the samples with $x = 0$, 0.3, 0.5, and 0.8, respectively, favoring the appearance of P_{disp}. Third, it is known that Ir ions can exist in trivalent or tetravalent forms. In order to check the valence of Ir ions, $SrMg_xIr_xFe_{12-2x}O_{19}$ ceramics are investigated by XPS technique. The typical binding energy of Ir $4f_{7/2}$ is expected to be about 61.8 eV for Ir^{4+} and 62.6 eV for Ir^{3+} [34]. Figure S2 of the Supplemental Material shows the Ir $4f_{7/2}$ XPS spectra of $SrMg_xIr_xFe_{12-x}O_{19}$ ceramics [33]. Though the binding energy peaks are not smooth enough due to the small Ir concentration, they are all located around 61.8 eV, indicating the valence state of Ir is dominated by 4+ in $SrMg_xIr_xFe_{12-2x}O_{19}$ ceramics. As shown in Table I, Ir^{4+} ions mainly substitute Fe^{3+} ions at $4f_2$ and $12k$ sites, and the main $4f_2$-site occupation of Ir^{4+} ions (with large ζ and orbital moment) can effectively change the magnetic interaction and enhance the local DMI [the $\boldsymbol{D}$ vector in the ab plane, Fig. 1(c)] between the $2b$ and $4f_2$ layers, which finally benefits the formation of conical spin order with the propagation vector $\boldsymbol{k}$ along the c axis. While as shown in Fig. 1(c), the $12k$-site Ir^{4+} ion has a complex effect because it can interact with three

TABLE I. Parameters from the Rietveld refinement of $SrMg_xIr_xFe_{12-2x}O_{19}$ ceramics.

x	R_{wp}(%)	R_p(%)	a(Å)	c(Å)	z_{2b}(Å)	2a site Fe/Mg/Ir ratio (%)	2b site Fe/Mg/Ir ratio (%)	4f_1 site Fe/Mg/Ir ratio (%)	4f_2 site Fe/Mg/Ir ratio (%)	12k site Fe/Mg/Ir ratio (%)	Spin-up site net substituted ratio (%)
0	4.68	3.56	5.88133(10)	23.0610(5)	0.048(13)	88(3)/	92(16)/	94(17)/	93(19)/	97(10)/	1.5%
0.3	3.59	2.58	5.88561(8)	23.0467(4)	0.065(19)	10(2)/	8(16)/	6(17)/	0(17)/	0(10)/	
						2(6)	0(4)	0(4)	7(8)	3(2)	
0.5	3.71	2.68	5.89124(7)	23.0288(4)	0.120(12)	86(8)/	90(16)/	86(19)/	89(19)/	96(8)/	−0.3%
						12(8)/	9(15)/	14(19)/	0(19)/	0(8)/	
						2(7)	1(4)	0(4)	11(9)	4(2)	
0.8	4.20	2.87	5.89487(9)	23.0201(5)	0.056(18)	60(12)/	90(18)/	81(17)/	83(16)/	93(12)/	2.5%
						34(12)/	9(16)/	18(16)/	0(15)/	0(12)/	
						6(10)	1(5)	1(3)	17(3)	7(3)	

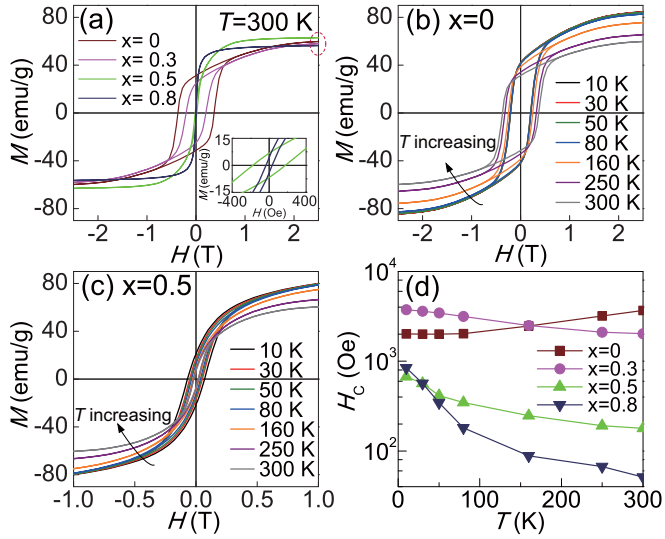

FIG. 2. Magnetic hysteresis loops of (a) $SrMg_xIr_xFe_{12-2x}O_{19}$ ceramics at room temperature and (b) $SrFe_{12}O_{19}$ and (c) $SrMg_{0.5}Ir_{0.5}Fe_{11}O_{19}$ ceramics with various temperatures. (d) T-dependent H_c of $SrMg_xIr_xFe_{12-2x}O_{19}$ ceramics. The inset gives the enlarged parts of magnetic hysteresis loops for the samples with $x = 0.5$ and 0.8.

Fe^{3+} sites (12k, 4f_1, and 4f_2) geometrically. The competition between the additional 12k-12k DMI and the interlayer DMI (12k-4f_1 and 12 k-4f_2) can disturb the conical spin order propagating along the c axis. That is to say, Ir^{4+} substitution at the 12k site is unhelpful to a conical magnetic structure. Finally, unlike Ir^{4+} ions, nonmagnetic Mg^{2+} ions, possessing no SOC and entering the sites (2a and 4f_1, Table I) with different spin directions, show negligible effect on the formation of conical spin order [3]. While the Mg^{2+} ion at the 2a site, that is adjacent to the 2b site along the c axis, can squeeze the 2b−site space due to its larger radius than that of the Fe^{3+} ion, and thus cause the reduction of z_{2b}. In addition, the enhanced DMI of the Fe^{3+}(2b)-O^{2-}-Ir^{4+}(4f_2) triad requires the Fe^{3+}(2b)-O^{2^-} and O^{2^-}-Ir^{4+}(4f_2) bond angles closer to 90 ° to reduce the system energy [35], tending to increase z_{2b}. The competition between the above two factors makes z_{2b} first increase as x increases from $x = 0$ to 0.5 and then decrease for $x = 0.8$. Taken together, Ir^{4+} ions mainly enter the crucial 4f_2 magnetic-interaction site and can simultaneously tune the magnetic and lattice structures of $SrMg_xIr_xFe_{12-2x}O_{19}$.

B. Magnetization measurements

Figure 2(a) exhibits the room-temperature magnetic hysteresis loops of $SrMg_xIr_xFe_{12-2x}O_{19}$ ceramics. Compared with pure $SrFe_{12}O_{19}$, the saturation magnetization (M_s) decreases for the samples with $x = 0.3$ and 0.8 while it increases for $x = 0.5$. In ferrimagnetic $SrFe_{12}O_{19}$, the spins of 16 Fe^{3+} ions at 12k, 2a, and 2b are spin-up and antiparallel to those of the 8 Fe^{3+} ions at the 4f_1 and 4f_2 sites, leading to a net moment of 40 μ_B per unit cell [36]. When Mg^{2+} and Ir^{4+} ions are introduced in $SrFe_{12}O_{19}$, their different magnetic moments and net effective substitution to spin-up or spin-down Fe^{3+} can affect the magnetization of $SrFe_{12}O_{19}$. The net effective

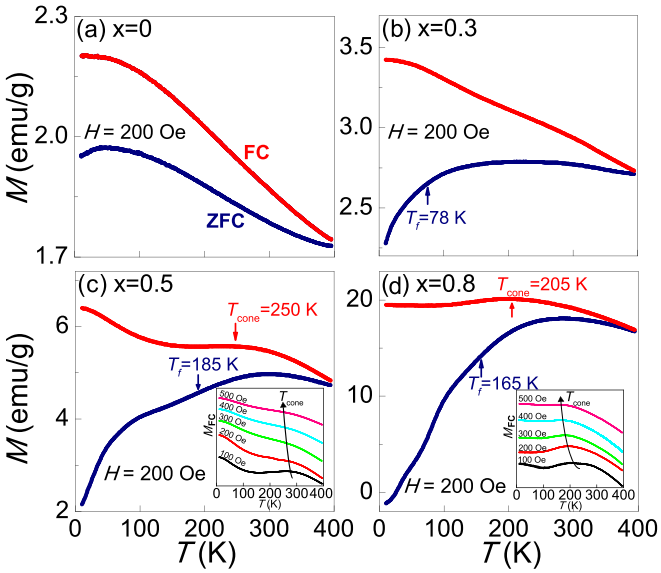

FIG. 3. T-dependent M of $SrMg_xIr_xFe_{12-2x}O_{19}$ ceramics under ZFC and FC conditions with $H = 200$ Oe. The inset gives T-dependent M_{FC} under different H for the samples with $x = 0.5$ and $x = 0.8$.

substitution to the Fe^{3+} ions of the spin-up site with nonmagnetic Mg^{2+} and weak-magnetic Ir^{4+} ions is responsible for the decreased M_s of the ceramics with $x = 0.3$ and 0.8. While for the samples with $x = 0.5$, the preferred substitution at spin-down ($4f_1$ and $4f_2$) sites (Table I) results in the slightly increased M_s. Based on the different magnetic moments of Fe^{3+} ($\sim 5\,\mu_B$) and Ir^{4+} ($\sim 1.5\,\mu_B$) [37] and their fractional occupancies determined from XRD analysis (Table I), the magnetic moments estimated by adding up the moments of Fe^{3+} and Ir^{4+} are $40.0\,\mu_B$, $39.0\,\mu_B$, $40.4\,\mu_B$, and $38.4\,\mu_B$, respectively, for the ceramics with $x = 0$, 0.3, 0.5, and 0.8. The evolution of the magnetic moment keeps in accord with that of the spin-up site net substituted ratio (the number of Fe^{3+} ions substituted at the $2a$, $2b$, and $12k$ sites subtracting that at the $4f_1$ and $4f_2$ sites, then divided by the total number of $2a$, $2b$, and $12k$ sites, shown in Table I) and M_s. More important, the introduction of Ir^{4+} and Mg^{2+} ions dramatically decreases the coercive field (H_c), which decreases from 3738 Oe for $x = 0$ to 179 and 55 Oe, respectively, for the ceramics with $x = 0.5$ and 0.8. This represents the rapid decline of uniaxial magnetocrystalline anisotropy, favoring the formation of conical spin order. Figures 2(b) and 2(c) show the magnetic hysteresis loops of the $SrFe_{12}O_{19}$ and $SrMg_{0.5}Ir_{0.5}Fe_{11}O_{19}$ ceramics at various temperatures. Unlike the decreased H_c for pure $SrFe_{12}O_{19}$, the H_c of all doped $SrMg_xIr_xFe_{12-2x}O_{19}$ ceramics gradually increases with decreasing temperature (T) [Fig. 2(d)], implying the difference of their interaction.

Figure 3 demonstrates the T dependence of magnetization (M) under zero field cooled (ZFC) and field cooled (FC) conditions with external magnetic field (H) of 200 Oe. The FC magnetization (M_{FC}) of the ceramics with $x = 0$ and 0.3 exhibits a typical ferrimagnetic feature, that is, M_{FC} monotonically increases with decreasing T. However, the M_{FC} curves display obvious anomalies around 250 and 205 K, respectively, for the samples with $x = 0.5$ and 0.8. From such temperature, M_{FC} stops increasing and even starts to slightly decrease with decreasing T, indicating the collinear ferrimagnetic spin order starts to transform to conical spin order at the temperature (T_{cone}) [1,20], below which the conical spin projections onto the cone bottom balance themselves out, and make smaller M_{FC} left due to the increased cone angle [38]. Moreover, as shown in the insets of Figs. 3(c) and 3(d), T_{cone} shifts to lower T and the transformation becomes inconspicuous under larger external H, similar to that observed in ME $Ba(Fe, Sc, In)_{12}O_{19}$ polycrystals [3,39]. In order to confirm the appearance of conical spin order, $SrMg_{0.5}Ir_{0.5}Fe_{11}O_{19}$ single-crystal platelets grown along the ab plane were prepared (Fig. S3) [33]. As shown in Fig. S4 [33], the M_{FC} of $SrMg_{0.5}Ir_{0.5}Fe_{11}O_{19}$ single crystal under $H \parallel c$ condition decreases with decreasing temperature below 313 K and shows a sharp decrease below 135 K, similar to the results reported in $BaFe_{12-x}Sc_xMg_{0.05}O_{19}$ single crystal [1], where conical spin order is evidenced by neutron diffraction and the sharp decrease corresponds to the rapid increase of the cone angle. Therefore, it is reasonable to believe that conical spin order is induced in $SrMg_{0.5}Ir_{0.5}Fe_{11}O_{19}$ single crystal. However, the M_{FC} curve on the $H \perp c$ condition displays a typical feature of collinear ferrimagnetism. In other words, the spin order of $SrMg_{0.5}Ir_{0.5}Fe_{11}O_{19}$ single crystal differs under H applied in different directions relative to crystallographic orientation. The M_{FC} of $SrMg_xIr_xFe_{12-2x}O_{19}$ ($x = 0.5$ and 0.8) ceramics can be regarded as a superposed signal contributed by both collinear and conical spin orders. With decreasing T, their M_{FC} does not display a prominent decrease below T_{cone} due to the increasing M_{FC} signal from the collinear spin part. As mentioned above, the emergence of conical spin order is dominated by Ir^{4+} substitution at the $4f_2$ site. For the samples with $x = 0.5$, Ir^{4+} ions at the crucial $4f_2$ site are sufficient for the formation of conical spin order. Then, more Ir^{4+} ions enter the $12k$ site with increasing x and disturb the conical spin order, causing a decreased T_{cone} for the samples with $x = 0.8$. In short, compared with other ionic doping [1–3], Ir^{4+} doping with a relatively low substitution level (about 4.2% of the total Fe^{3+} ions) can effectively induce conical spin order in $SrFe_{12}O_{19}$ because of its strengthened SOC.

M_{ZFC} and the difference between M_{ZFC} and M_{FC} also show differences among different $SrMg_xIr_xFe_{12-2x}O_{19}$ ceramics. As shown in Fig. 3, the difference between M_{ZFC} and M_{FC} becomes more obvious with increasing x, and meanwhile, the M_{ZFC} rapidly decreases below freezing temperature (T_f) for the samples with $x = 0.5$ and 0.8, implying the appearance of spin-glass state. Such behavior commonly exists in M-type hexaferrite systems with conical spin order [3,20], where the antiferromagnetic interaction deviates from the c axis. Meanwhile, when partial Fe^{3+} ions are substituted by Ir^{4+} and Mg^{2+} ions in $SrFe_{12}O_{19}$, the antiferromagnetic interactions among Fe^{3+} ions are affected or interrupted. Consequently as Fig. S5 [33] shows, local nanomagnetic domain appears, and the correlation among them increases with decreasing T and thus gives rise to ferromagnetic exchange coupling at low temperature. The competition between ferromagnetic and tilting antiferromagnetic interaction below T_{cone} is responsible for the formation of a spin-glass state. For the samples with $x = 0.3$, though an obvious conical spin structure does not

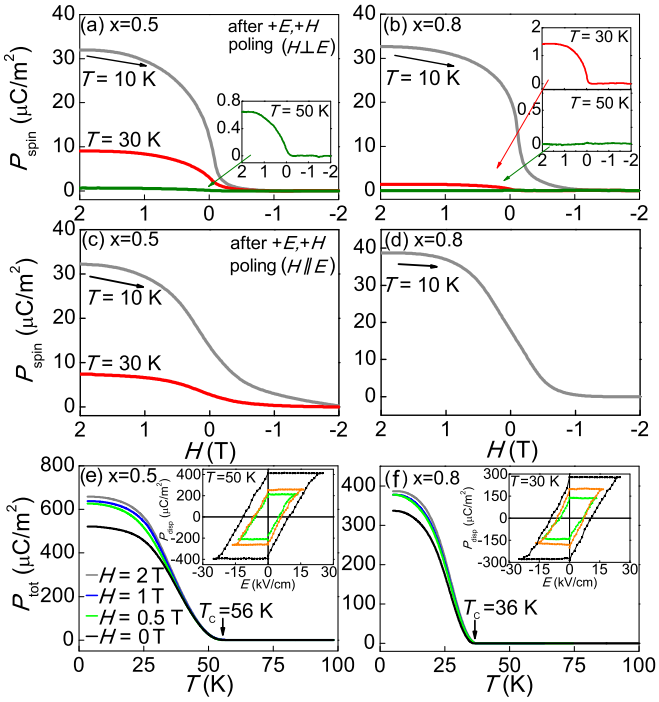

FIG. 4. The relative P_{spin} of $SrMg_xIr_xFe_{12-2x}O_{19}$ ceramics: (a) $x = 0.5$ and (b) $x = 0.8$ on $H \perp E$ condition and (c) $x = 0.5$ and (d) $x = 0.8$ on $H \parallel E$ condition. P_{tot} of $SrMg_xIr_xFe_{12-2x}O_{19}$ ceramics on $H \perp E$ condition: (e) $x = 0.5$ and (f) $x = 0.8$. The insets of (a) and (b) give the detailed P_{spin} and the insets of (e) and (f) give the PUND ferroelectric hysteresis loops below T_C, respectively.

appear due to the lesser Ir^{4+} substitution, a spin-glass state also exists probably because of the destruction of long-range collinear spin order. The freeze of spin glass in $SrMg_xIr_xFe_{12-2x}O_{19}$ ceramics contributes to their enhancement of H_c with decreasing T [Fig. 2(d)].

C. ME effect

ME effect is taken for granted in $SrMg_xIr_xFe_{12-2x}O_{19}$ ($x = 0.5$ and 0.8) ceramics with conical spin order. The direct coupling between magnetic and ferroelectric orders (i.e., ME coupling) can be confirmed by P_{spin}. The samples were first prepolarized with $H = +2$ T and electric field ($E = +16.67$ kV/cm) under $H \perp E$ or $H \parallel E$ condition. Then, the electric field was cut off and the electrodes were shorted for 30 min before collecting ME current via sweeping H from 2 to -2 T. Figures 4(a)–4(d) exhibit the relative polarization of the samples with $x = 0.5$ and 0.8 in T range of 10–50 K, where the polarization is defined as zero when H reaches -2 T. In comparison, no obvious ME current and thus polarization can be detected for the samples with $x = 0$ and $x = 0.3$ at any T (Fig. S6 [33]), implying the polarization stems from the conical spin order, i.e., P_{spin}. Moreover, the relative P_{spin} exhibits a prominent decline around H_c on $H \perp E$ condition, and its magnitude reduces gradually as T increases, and finally vanishes above 50 and 30 K for the ceramics with $x = 0.5$ and 0.8, respectively [Figs. 4(a) and 4(b)]. On $H \parallel E$ condition, similar results are observed for $SrMg_xIr_xFe_{12-2x}O_{19}$ ($x = 0.5$ and 0.8) ceramics except that the relative P_{spin} changes more slowly due to the larger geometric demagnetizing factor [Figs. 4(c) and 4(d)].

The inverse DMI model, where $\boldsymbol{P}_{\text{spin}} \propto \sum \boldsymbol{k} \times (\boldsymbol{S}_i \times \boldsymbol{S}_j)$ and $\boldsymbol{k}$ is the propagation vector of spiral spin order, forbids a P_{spin} component parallel to $\sum \boldsymbol{S}_i \times \boldsymbol{S}_j$ (the same direction with $\boldsymbol{H}$) [18]. Therefore, the comparable value of P_{spin} under $P \perp H$ and $P \parallel H$ conditions implies that the ME effect of $SrMg_xIr_xFe_{12-2x}O_{19}$ ($x = 0.5$ and 0.8) originates from the d-p hybridization mechanism, in which P_{spin} is given by [19]

$$\boldsymbol{P}_{\text{spin}} = \sum p_{il} \boldsymbol{e}_{il} (\boldsymbol{e}_{il} \cdot \boldsymbol{S}_i)^2, \tag{1}$$

where $\boldsymbol{e}_{il}$ denotes the unit vector connecting magnetic ionic site i to its neighboring ligand site l and p_{il} is a constant related to SOC. In d-p hybridization, P_{spin} calls for the coexistence of conical spin order and a special lattice form with broken inversion symmetry [40]. Thus, P_{spin} is only allowed in the FeO_5 trigonal bipyramid ($2b$ site) and/or FeO_4 tetrahedra ($4f_1$ site) of M-type hexaferrite. Considering the main $4f_2$-site substitution of Ir^{4+} ions and the strong interaction between $2b$ and $4f_2$ sites, the $2b$ site should be the main contributing site of P_{spin}. Such speculation can be confirmed by pyroelectric measurement. The samples were cooled from room temperature to 5 K under $E = +16.67$ kV/cm and $H = 0-2$ T ($H \perp E$) condition, and then the electrodes were shorted for 30 min. Pyroelectric current was collected by heating the samples with 4 K/min and the total ferroelectric polarization (P_{tot}) is integrated by pyroelectric current. Figures 4(e) and 4(f) shows the $T-$dependent P_{tot} with different H, and there are three features worth mentioning. First, under zero magnetic field, the cone axis is along the easy magnetization c axis [Fig. 1(c)], and such longitudinal conical structure has no net P_{spin} because of the canceled spin projections on the ab plane and thus the vanishing summation of $\boldsymbol{P}_{\text{spin}} = \sum p_{il} \boldsymbol{e}_{il} (\boldsymbol{e}_{il} \cdot \boldsymbol{S}_i)^2$. Instead, P_{spin} can be readily induced by tilting the cone axis with H. That is to say, the applied H is a precondition to P_{spin}. Therefore, the polarizations under zero and nonzero H correspond to P_{disp} and P_{tot} (the sum of P_{disp} and P_{spin}), respectively. With increasing T, P_{disp} gradually decreases to zero at Curie temperature T_C, which is 56 and 36 K, respectively, for the samples with $x = 0.5$ and 0.8. Below T_C, the PUND ferroelectric hysteresis loops shown in the insets of Figs. 4(e) and 4(f) further confirm the displacive ferroelectricity. To be sure, pyroelectric current was collected by heating the samples after removing the poling electric field, and thus the corresponding ferroelectric polarization mainly comes from the remanent polarization part, while the polarization measured by the PUND method is all the switchable ferroelectric polarization. Therefore, at the same temperature and electric field, P_{disp} measured by PUND is usually larger than that by pyroelectric current. T_C approaches the vanishing temperature of P_{spin} for the samples with $x = 0.5$ and 0.8. Such synergy variation indicates that P_{disp} and P_{spin} couple with each other and confirms that the d-p hybridization emerges at FeO_5 trigonal bipyramids ($2b$ site). That is to say, the main SOC originates from the $2b$ site with the ionic off-center displacement and thus asymmetric crystal field. Second, the displaced ions can rapidly oscillate between the two equivalent positions once the thermal energy is greater than the energy barrier of the up and down positions, causing the vanishing of polarization [12–14]. That is, though nonzero

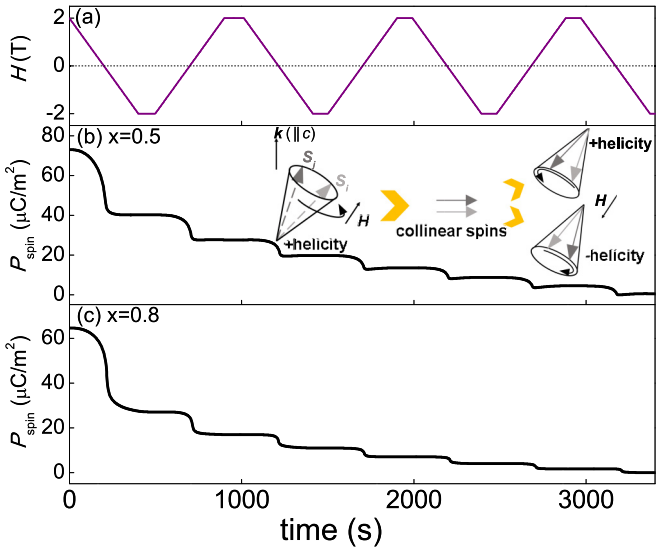

FIG. 5. P_{spin} response of $SrMg_xIr_xFe_{12-2x}O_{19}$ ceramics ($x = 0.5$ and 0.8) via sweeping H periodically on the $H \perp E$ condition at 10 K. The inset gives a schematic of helicity loss.

z_{2b} is observed at room temperature, T_C usually appears below room temperature. Moreover, compared with that of the ceramics with $x = 0.8$, both P_{tot} and T_C of the samples with $x = 0.5$ are higher because of its larger z_{2b} (Table I). Third, P_{tot} increases with increasing H and gradually reaches saturation after 1 T, further confirming the regulating effect of H on polarization. In short, the ME effect of $SrMg_xIr_xFe_{12-2x}O_{19}$ not only depends on the conical spin order, but also on z_{2b}. Furthermore, compared with the In^{3+}-doped M-type hexaferrite [3], Ir^{4+} doping with lower substitution level can effectively induce a conical magnetic structure in $SrFe_{12}O_{19}$ and lift the magnitude of P_{spin} by about two orders on account of its strong SOC. It should be mentioned that though the large SOC of Ir^{4+} is beneficial for the enhancement of ME coupling, conical spiral structure is the prerequisite for its appearance. Figure S7 [33] shows the XAS spectra of the ceramics with $x = 0.3$ and 0.5. It is seen that SOC occurs in both ceramics, but ME coupling is only observed in the ceramics with $x = 0.5$, further confirming the appearance of the conical spin structure in $SrMg_{0.5}Ir_{0.5}Fe_{11}O_{19}$.

The P_{spin} response of $SrMg_xIr_xFe_{12-2x}O_{19}$ ($x = 0.5$ and 0.8) ceramics is further tested by periodic H on $H \perp E$ condition at 10 K, and is shown in Fig. 5. Unlike the retrievable P_{spin} common in other hexaferrite systems [1,6,41], the relative P_{spin} response of $SrMg_xIr_xFe_{12-2x}O_{19}$ displays an interesting decline behavior with an increasing cycle of H, where P_{spin} is defined as zero when the last sweep ends. To explain such behavior, one should take insight on the principles of the ME coupling test. P_{spin} of $SrMg_xIr_xFe_{12-2x}O_{19}$ ($x = 0.5$ and 0.8) is connected with conical spin order, whose helicity $\sum \boldsymbol{k} \cdot (\boldsymbol{S}_i \times \boldsymbol{S}_j)$ defines its polar state. The $+E$, $+H$ prepolarization not only determines $+P_{spin}$, but also selects the sign of helicity to satisfy $+P_{spin}$. In general hexaferrite, the sign of helicity keeps accord with M on H reversal, causing retrievable P_{spin} when repeatedly sweeping H [1,6,41]. The decreasing P_{spin} in $SrMg_xIr_xFe_{12-2x}O_{19}$ ($x = 0.5$ and 0.8) suggests an irretrievable helicity on H reversal. Unlike the retentive conical spin order of $BaSc_xFe_{12-x}O_{19}$ single crystals on $H \perp c$ condition [1], the characteristic of collinear spin order is observed on this condition for the $SrMg_{0.5}Ir_{0.5}Fe_{11}O_{19}$ single-crystal platelet. Therefore, as shown in the inset schematic of Fig. 5(b), the sign of helicity may not be restricted in $SrMg_xIr_xFe_{12-2x}O_{19}$ if an intermediate state of collinear spin order emerges on H reversal. Therefore, every time H reverses, the helicity gets more random and finally approaches zero. Thus, P_{spin} displays a macroscopical decline as the measurement cycle increases, and finally reflects the multilevel magnetoelectric states. It should be mentioned that the helicity and P_{spin} can be polarized to the initial state again after $+E$, $+H$ polarization.

IV. CONCLUSION

In summary, we have investigated the structural, magnetic, and ME properties of $SrMg_xIr_xFe_{12-2x}O_{19}$. A conical magnetic structure is induced in $SrMg_xIr_xFe_{12-2x}O_{19}$ ceramics by a small amount of Ir^{4+} doping (about 4.2% of the total Fe^{3+} ions) because Ir^{4+} ions with large SOC prefer to enter the crucial $4f_2$ sublattice and thus enhance the local DMI. As a result, enhanced P_{spin} in $SrMg_xIr_xFe_{12-2x}O_{19}$ ($x = 0.5$ and 0.8) ceramics is obtained and considered to originate from the d-p hybridization mechanism, which emerges at FeO_5 trigonal bipyramids and couples with P_{disp}. Moreover, P_{spin} decreases step by step with a periodical ME test due to helicity loss. These results provide a feasible avenue to develop and enhance the ME coupling of a M-type hexaferrite system, and offer a clue to multilevel states storage.

ACKNOWLEDGMENTS

This work was supported by National Natural Science Foundation of China (Grants No. 62171214, No. 52172116, No. 11874208, and No. 51721001) and the Priority Academic Program Development of Jiangsu Higher Education Institutions (PAPD).

[1] Y. Tokunaga, Y. Kaneko, D. Okuyama, S. Ishiwata, T. Arima, S. Wakimoto, K. Kakurai, Y. Taguchi, and Y. Tokura, Phys. Rev. Lett. **105**, 257201 (2010).

[2] L. Y. Wang, D. H. Wang, Q. Q. Cao, Y. X. Zheng, H. C. Xuan, J. L. Gao, and Y. W. Du, Sci. Rep. **2**, 223 (2012).

[3] Y. Shao, F. Z. Huang, J. T. Zhang, S. Yan, S. Y. Xiao, X. M. Lu, and J. S. Zhu, Adv. Quantum Technol. **4**, 2000096 (2021).

[4] T. Nakajima, Y. Tokunaga, M. Matsuda, S. Dissanayake, J. Fernandez-Baca, K. Kakurai, Y. Taguchi, Y. Tokura, and T.-h. Arima, Phys. Rev. B **94**, 195154 (2016).

[5] Y. Umimoto, N. Abe, S. Kimura, Y. Tokunaga, and T.-h. Arima, Phys. Rev. B **101**, 100403(R) (2020).

[6] Y. S. Chai, S. H. Chun, J. Z. Cong, and K. H. Kim, Phys. Rev. B **98**, 104416 (2018).

[7] Y. Kitagawa, Y. Hiraoka, T. Honda, T. Ishikura, H. Nakamura, and T. Kimura, Nat. Mater. **9**, 797 (2010).

[8] M. Soda, T. Ishikura, H. Nakamura, Y. Wakabayashi, and T. Kimura, Phys. Rev. Lett. **106**, 087201 (2011).

[9] R. C. Pullar, Prog. Mater. Sci. **57**, 1191 (2012).

[10] W. D. Townes, J. H. Fang, and A. J. Perrotta, Z. Kristallogr., Kristallgeom., Kristallphys., Kristallchem. **125**, 437 (1967).

[11] J. G. Rensen and J. S. van Wieringen, Solid State. Commun. **7**, 1139 (1969).

[12] H. B. Cao, Z. Y. Zhao, M. Lee, E. S. Choi, M. A. McGuire, B. C. Sales, H. D. Zhou, J. Q. Yan, and D. G. Mandrus, APL Mater. **3**, 062512 (2015).

[13] S. P. Shen, Y. S. Chai, J. Z. Cong, P. J. Sun, J. Lu, L. Q. Yan, S. G. Wang, and Y. Sun, Phys. Rev. B **90**, 180404 (2014).

[14] P. S. Wang and H. J. Xiang, Phys. Rev. X **4**, 011035 (2014).

[15] J. E. Beevers, C. J. Love, V. K. Lazarov, S. A. Cavill, H. Izadkhah, C. Vittoria, R. Fan, G. van der Laan, and S. S. Dhesi, Appl. Phys. Lett. **112**, 082401 (2018).

[16] Y. Shao, F. Z. Huang, X. Y. Xu, S. Yan, C. B. Yang, M. Zhou, X. M. Lu, and J. S. Zhu, Appl. Phys. Lett. **114**, 242902 (2019).

[17] H. Katsura, N. Nagaosa, and A. V. Balatsky, Phys. Rev. Lett. **95**, 057205 (2005).

[18] C. D. Hu, Phys. Rev. B **77**, 174418 (2008).

[19] T.-h. Arima, J. Phys. Soc. Jpn. **76**, 073702 (2007).

[20] S. Gupta, S. K. Upadhyay, V. Siruguri, V. G. Sathe, and E. V. Sampathkumaran, J. Phys.: Condens. Matter. **31**, 295701 (2019).

[21] S. Gupta, V. G. Sathe, and V. Siruguri, J. Alloy. Compd. **825**, 154141 (2020).

[22] I. Dzyaloshinsky, J. Phys. Chem. Solids **4**, 241 (1958).

[23] T. Moriya, Phys. Rev. **120**, 91 (1960).

[24] A. S. Moskvin, J. Exp. Theor. Phys. **104**, 913 (2007).

[25] C. Tejera-Centeno, S. Gallego, and J. I. Cerda, Sci. Rep. **11**, 1964 (2021).

[26] D. Kan, M. Mizumaki, M. Kitamura, Y. Kotani, Y. Shen, I. Suzuki, K. Horiba, and Y. Shimakawa, Phys. Rev. B **101**, 224434 (2020).

[27] C. B. Park, K. W. Shin, S. H. Chun, J. H. Lee, Y. S. Oh, S. M. Disseler, C. A. Heikes, W. D. Ratcliff, W.-S. Noh, J.-H. Park, and K. H. Kim, Phys. Rev. Mater. **5**, 034412 (2021).

[28] J. Kreisel, H. Vincent, F. Tasset, M. Pate, and J. P. Ganne, J. Magn. Magn. Mater. **224**, 17 (2001).

[29] B. J. Kim, H. Jin, S. J. Moon, J. Y. Kim, B. G. Park, C. S. Leem, J. Yu, T. W. Noh, C. Kim, S. J. Oh, J. H. Park, V. Durairaj, G. Cao, and E. Rotenberg, Phys. Rev. Lett. **101**, 076402 (2008).

[30] B. J. Kim, H. Ohsumi, T. Komesu, S. Sakai, T. Morita, H. Takagi, and T.-h. Arima, Science **323**, 1329 (2009).

[31] D. Pesin and L. Balents, Nat. Phys. **6**, 376 (2010).

[32] J. P. Clancy, N. Chen, C. Y. Kim, W. F. Chen, K. W. Plumb, B. C. Jeon, T. W. Noh, and Y.-J. Kim, Phys. Rev. B **86**, 195131 (2012).

[33] See Supplemental Material at http://link.aps.org/supplemental/10.1103/PhysRevB.106.144419 for the SEM images of $SrMg_xIr_xFe_{12-2x}O_{19}$ ceramics, the XPS data of $SrMg_xIr_xFe_{12-2x}O_{19}$ ($x = 0.3$, 0.5, and 0.8) ceramics, the preparation, structural and magnetic properties of $SrMg_{0.5}Ir_{0.5}Fe_{11}O_{19}$ single-crystal platelets, the MFM images of $SrMg_xIr_xFe_{12-2x}O_{19}$ ($x = 0.5$ and 0.8) ceramics, the ME current of $SrMg_xIr_xFe_{12-2x}O_{19}$ ($x = 0$ and 0.3) ceramics, and the XAS data of $SrMg_xIr_xFe_{12-2x}O_{19}$ ($x = 0.3$ and 0.5) ceramics.

[34] R. Kötz, H. Neff, and S. Stucki, J. Electrochem. Soc. **131**, 72 (1984).

[35] C. J. Fennie, Phys. Rev. Lett. **100**, 167203 (2008).

[36] M. Awawdeh, I. Bsoul, and S. H. Mahmood, J. Alloy. Compd. **585**, 465 (2014).

[37] M. Wakeshima, N. Taira, Y. Hinatsu, and Y. Ishii, Solid State Commun. **125**, 311 (2003).

[38] O. P. Aleshko-Ozhevskii and I. I. Yamzin, J. Exp. Theor. Phys. **29**, 655 (1969).

[39] A. Hilczer, K. Pasińska, B. Andrzejewski, M. Matczak, and A. Pietraszko, Ceram. Int. **45**, 1189 (2019).

[40] Y. Tokura, S. Seki, and N. Nagaosa, Rep. Prog. Phys. **77**, 076501 (2014).

[41] H. Ueda, Y. Tanaka, Y. Wakabayashi, and T. Kimura, Phys. Rev. B **100**, 094444 (2019).